

# Characterization of Control in a Superconducting Qutrit Using Randomized Benchmarking

M. Kononenko,<sup>1, 2, \*</sup> M.A. Yurtalan,<sup>1, 2, †</sup> J. Shi,<sup>1, 2</sup> and A. Lupascu<sup>1, 2, 3, ‡</sup>

<sup>1</sup>*Institute for Quantum Computing, University of Waterloo, Waterloo, ON, Canada, N2L 3G1*

<sup>2</sup>*Department of Physics and Astronomy, University of Waterloo, Waterloo, ON, Canada, N2L 3G1*

<sup>3</sup>*Waterloo Institute for Nanotechnology, University of Waterloo, Waterloo, ON, Canada N2L 3G1*

(Dated: December 22, 2024)

We present experimental results on the characterization of control fidelity for a qutrit implemented in the lowest three levels of a capacitively shunted flux-biased superconducting circuit. Using randomized benchmarking, we measure an average fidelity over the elements of the qutrit Clifford group of  $99.0 \pm 0.2\%$ . In addition, for a selected subset of the Clifford group, we characterize the fidelity using quantum process tomography, and by observing the periodic behaviour of repeated gate sequences. We use a general method for implementation of qutrit gates, that can be used to generate any unitaries based on two-state rotations. The detailed analysis of the results indicates that errors are dominated by ac-Stark and Bloch-Siegert shifts. This work demonstrates the ability for high-fidelity control of qutrits and outlines interesting avenues for future work on optimal control of single and multiple superconducting qudits.

Recent advances in large-scale quantum information processors have relied on manipulating quantum information using two-level systems as qubits [1–4]. Theoretical work shows that using multilevel systems as qudits offers performance advantages in quantum error correction [5–8], quantum sensing [9, 10], and quantum communication [11]. Efficient universal qudit control required for these applications follows from an extension of the Solovay-Kitaev theorem from the qubit unitary group  $SU(2)$  to the qudit group  $SU(d)$ , where  $d$  is the dimension of the qudit’s Hilbert space [12]. However, implementation of such control brings new challenges including mapping qudit gates to experimentally-accessible controls, and understanding how control errors influence the type and amount of errors in a qudit gate. Characterizing qudit gates is also more resource-intensive than characterizing qubit gates since the larger Hilbert space allows more complex states to form.

In this paper, we characterize qutrit control using randomized benchmarking (RB). RB is a protocol that yields the average error for the elements of the Clifford group. We implement qutrit gates using a universal decomposition method that can be used to generate any unitary. The measured average fidelity  $\bar{\mathcal{F}} = 99.0 \pm 0.2\%$  for members of the qutrit Clifford group  $\mathcal{C}_3$ . In addition, we characterize a subset of the Clifford group using quantum process tomography, which provides an independent verification of the unitary synthesis method and yields results in agreement with RB. Our analysis of this experiment revealed errors due to level shifts, leakage, and decoherence. The experiment and the analysis underline the relevance of level shifts, which does not lead to significant errors in the usual case of resonant control in a two-dimensional subspace, and points to relevant future work on improved control pulses for qudits.

The experiment is performed on a variant of a capacitively-shunted flux qubit that combines relatively

long coherence times with high anharmonicity, with anharmonicity defined as the difference between the second and first transition frequency [13]. A qutrit is encoded in the lowest three energy states of the device, denoted by 0, 1, and 2. The large anharmonicity enables fast selective driving of the 0 – 1 and 1 – 2 transitions. Control of the qutrit is done using microwave pulses sent using a coplanar waveguide coupled capacitively to the device (see Fig. 1 (a)). Application of a microwave pulse resonant with the  $m - n$  transition implements a rotation  $R(\theta)_\phi^{nm}$  in the two dimensional space formed by states  $|m\rangle$  and  $|n\rangle$ , where  $\theta$  is the rotation angle and  $\phi$  is the phase of the rotation. Control pulses are generated using direct synthesis by a large bandwidth arbitrary waveform generator, model Tektronix AWG 70001. The device state is measured using homodyne readout of a coplanar waveguide resonator also coupled capacitively to the device. The readout voltage, averaged over many repetitions, corresponds to the expectation value of the operator  $V = V_0 |0\rangle\langle 0| + V_1 |1\rangle\langle 1| + V_2 |2\rangle\langle 2|$ . State preparation is done by waiting for the device to relax to the thermal state  $\rho_{\text{th}} = P_{\text{th},0} |0\rangle\langle 0| + P_{\text{th},1} |1\rangle\langle 1|$ , where  $P_{\text{th},n} = \langle n | \rho_{\text{th}} | n \rangle$ . We assume that higher state populations are negligible, in line with the large transition frequency between states 1 and 2.  $P_{\text{th},1}$  is measured by comparing the amplitude of two Rabi oscillations between 0 and 1. The first oscillation is done starting with the thermal state with populations in states 1 and 2 swapped, and the second oscillation is done starting the thermal state with 0 and 1 population swap followed by a 1 and 2 population swap prior to performing the Rabi oscillation. (see Supplemental Material and Ref. [13]). The voltage levels  $V_0$ ,  $V_1$ , and  $V_2$  are characterized by measuring  $\langle V \rangle$  for three reference states: the thermal state, the thermal state followed by swapping populations between 0 and 1, and the thermal state followed by swapping populations between 1 and 2, then swapping 0 and 1 (see Supplemen-

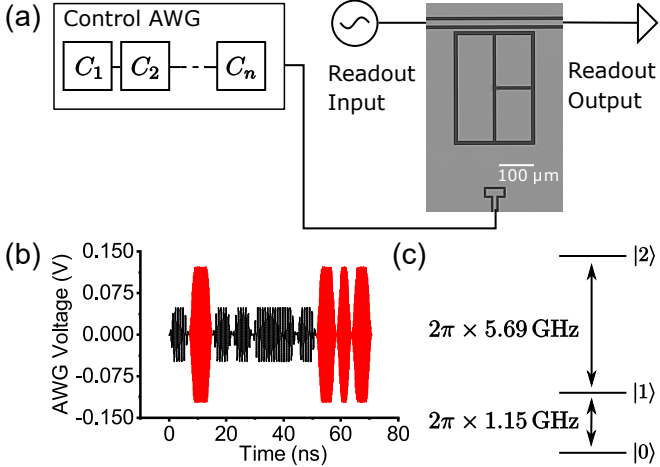


FIG. 1. A representation of the experiment setup. (a) A scanning electron micrograph of the device on which the experiment was performed, with connections to the control AWG and the readout setup shown. The control AWG is synthesizing a sequence of Clifford gates  $C_1$  to  $C_n$  for an RB experiment. (b) The waveform for a Walsh-Hadamard gate  $H_3$  as outputted by the control AWG. Black lines indicate  $0 - 1$  driven transitions and red lines indicate  $1 - 2$  driven transitions (c) A level diagram for the transitions used in the device. The transition frequencies are indicated.

tal Material and Ref. [13]).

Performing a qudit gate  $U$  requires a decomposition of  $U$  that can be mapped to the available controls, which becomes more difficult as  $d$  increases. In this paper we use an approach that decomposes  $U$  into products of Givens rotations  $R(\theta)_\phi^{mn}$ , where Givens rotations are unitaries in two-dimensional subspaces of the qudit space. This approach is universal for qudits of any dimension  $d$  and only requires the availability of Givens rotations for  $d - 1$  pairs of states that span the full Hilbert space [14]. The decomposition  $U$  has two main steps. In the first step, Givens rotations are identified that, when multiplying the unitary  $U$  in succession, lead to step-by-step cancellation of the off-diagonal elements of  $U$ , leading to a diagonal matrix. A maximum number of  $\frac{1}{2}d(d - 1)$  Givens rotations, one corresponding to cancellation of each element in the upper diagonal block, is required. In the second step,  $d - 1$  phase rotations are multiplying the resulting diagonal matrix, yielding the identity matrix up to a phase factor. Each of these rotations require three Givens rotations, for a total of  $3(d - 1)$  rotations. Additional details are discussed in the Supplemental Material. Decomposing a qutrit gate requires up to 9 Givens rotations. Each Givens rotation  $R(\theta)_\phi^{mn}$  is then mapped to a pulse generated by the AWG with the pulse envelope area proportional to  $\theta$ , the frequency resonant with the  $mn$  transition, and the phase given by  $\phi$ . The control Hamiltonian for  $R(\theta)_\phi^{mn}$  in the interaction picture is  $H_{\text{drive}} = \frac{1}{2}\Omega_{mn}e^{-i\phi}|m\rangle\langle n| + \text{h.c.}$ , where

$\Omega_{mn}$  is the drive strength for the  $m - n$  transition. Each pulse has a cosine-shaped rise and fall envelope with  $t_{\text{rise}} = t_{\text{fall}} = 2$  ns (See Supplemental Material). Figure 1 (b) shows the waveform for a qutrit Walsh-Hadamard gate  $H_3$  at  $\Omega_{01} = \Omega_{12} = 2\pi \times 50$  MHz synthesized using this decomposition [15].

The approach for implementing an arbitrary unitary is verified using quantum process tomography (QPT) for a set of representative gates, following the procedure from Ref. [15]. QPT is a standard technique for finding the process matrix of a black box [16], and so the gate fidelity [17] determined from the process matrix measures whether a qutrit gate performs as intended. We characterize the Walsh-Hadamard gate  $H_3$ , the generalized phase gate  $S_3$ , and the generalized Pauli gates  $X_3$  and  $Z_3$ .  $H_3$  and  $S_3$  were chosen since they generate the qutrit Clifford group  $\mathcal{C}_3$ .  $X_3$  and  $Z_3$  were chosen since they generate the Pauli group  $\mathcal{P}_3$  [18]. The gate fidelities for  $H_3$ ,  $S_3$ ,  $X_3$  and  $Z_3$  are 96.0%, 98.4%, 99.0%, and 99.0%, respectively, showing that the gate decomposition is synthesizing the intended gates.

Next, we characterized the average fidelity  $\bar{\mathcal{F}}$  of  $\mathcal{C}_3$  using RB. RB relies on the fact that a sequence of  $l$  random gates selected from  $\mathcal{C}_3$ , such that their product is nominally the identity, behaves on average as a depolarizing channel with the same  $\bar{\mathcal{F}}$  as  $\mathcal{C}_3$  [19, 20]. Therefore, measuring  $\langle V \rangle$  versus  $l$  determines  $\bar{\mathcal{F}}$  via the model

$$\langle V \rangle = (V_i - V_f) \left( \frac{d\bar{\mathcal{F}} - 1}{d - 1} \right)^l + V_f, \quad (1)$$

where  $V_i$  ( $V_f$ ) is  $\langle V \rangle$  at  $l = 0$  ( $l = \infty$ ), and  $d = 3$  is the dimension of the qudit [21]. RB is used since it measures  $\bar{\mathcal{F}}$  faster than QPT, at the expense of not giving information about individual gates in  $\mathcal{C}_3$  [20]. Based on the fact that  $H_d$  and  $S_d$  generate  $\mathcal{C}_d$  for any prime  $d$  [22], we generate the set  $\mathcal{C}_3$  by taking products of  $H_3$  and  $S_3$  until no new elements are obtained. Each Clifford gate used in RB is decomposed into Givens rotations using the decomposition presented above. Figure 2 (a) plots the experimentally-determined  $\langle V \rangle$  versus  $l$  for ten randomizations at each  $l \in \{2, 6, 10, 20, 50, 100, 200\}$ , with  $\Omega_{01} = \Omega_{12} = 2\pi \times 50$  MHz. The measured  $\bar{\mathcal{F}} = 99.0 \pm 0.2\%$  indicates that the members of  $\mathcal{C}_3$  are implemented to high fidelity on average. Uncertainties are quoted to one standard deviation. Increasing  $\Omega_{01}$  and  $\Omega_{12}$  to  $2\pi \times 97.38$  MHz leads to a reduced fidelity of  $97.3 \pm 0.3\%$ . Increasing rise and fall time from 2 ns to 3 ns does not improve  $\bar{\mathcal{F}}$ . Scaling the drive voltages by  $\pm 3\%$  to correct for possible over-rotations in 01 and 12 also does not significantly affect the fidelity, nor did it lead to a clear optimal result.

An important property of the elements of Clifford group is that they have a finite order, as implied by the fact that the group is finite. This order is a characteristic of each element. We performed experiments where the gates  $H_3$ ,  $S_3$ ,  $X_3$ , and  $Z_3$  were applied repeatedly to test

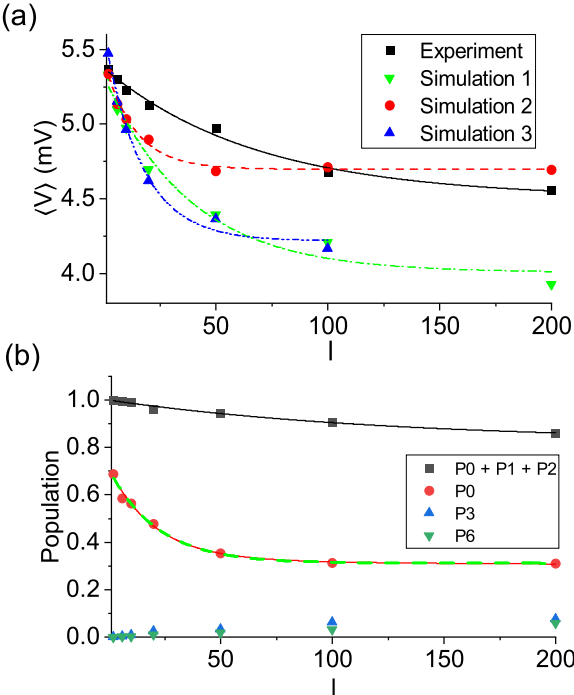


FIG. 2. Experiment and simulated results for qutrit RB. (a) The experimentally-measured  $\langle V \rangle$  compared to three simulation results. Simulation 1 is the numerically-simulated result. Simulation 2 is like Simulation 1, but with  $V_3$  and  $V_6$  optimized to match experiment data. Simulation 3 is like Simulation 1, but with decoherence modelled as well. Fits to equation 1 are shown for the experiment and each simulation. (b) The populations from Simulation 1 with the leakage analysis from [23] performed on them. The dashed line is the fitted  $P_0$  versus  $l$  with the small leakage approximation.

this periodic behaviour. For  $S_3$  and  $Z_3$ , an  $H_3$  gate was prepended and appended to the sequence to produce a  $\langle V \rangle$  signal varying with the repetition number  $N$ . Figure 3 shows the experimentally-measured  $\langle V \rangle$  versus the value expected from applying ideal gates to  $\rho_{\text{th}}$ . The experiments confirm the expected periodicity of these elements of the Clifford group. The deviation from the expected result increases with  $N$ , due to errors in control and decoherence.

We now discuss the sources of error in the experiment. Comparing results from the RB and QPT experiment, the fidelity from RB being slightly higher than the fidelity from QPT is consistent with RB being less sensitive to state preparation and measurement error than QPT [21]. In the RB experiment,  $V_i = 5.36 \pm 0.03$  mV matches  $\text{Tr}(V\rho_{\text{th}}) = 5.35 \pm 0.07$  mV and  $V_f = 4.50 \pm 0.07$  mV matches  $\text{Tr}(V\rho_{\text{dep}}) = 4.59 \pm 0.03$  mV, where  $\rho_{\text{dep}} = \frac{1}{3}(|0\rangle\langle 0| + |1\rangle\langle 1| + |2\rangle\langle 2|)$ . This is consistent with the RB sequence behaving as a depolarizing channel [21]. To analyze the RB results, we performed numerical simulations of the time dynamics of the system. We find the circuit parameters based on fitting spectroscopy to the

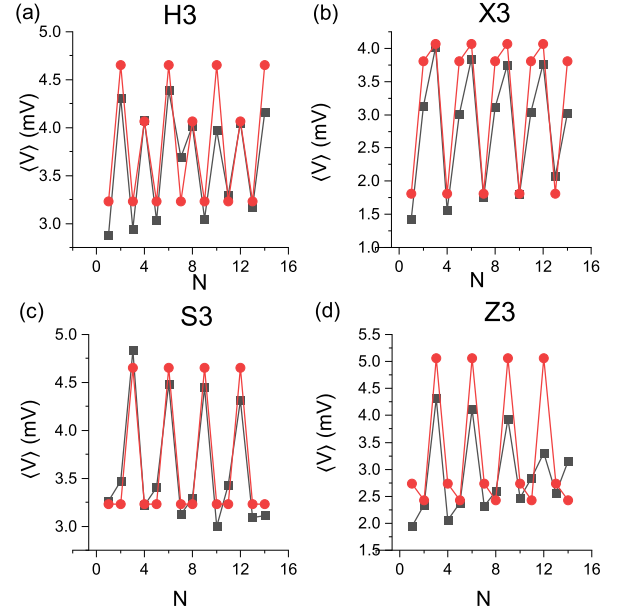


FIG. 3.  $\langle V \rangle$  versus  $N$  for repeated applications of  $H_3$ ,  $X_3$ ,  $S_3$ , and  $Z_3$ , shown in panels (a), (b), (c), and (d) respectively. The red circles are the expected  $\langle V \rangle$  versus  $N$  signal for the ideal gate, and the black squares are the experiment results.

circuit model (See Supplemental Material and Ref. [15]). We truncate the Hamiltonian to the seven lowest energy states, which was found to be sufficient to properly explain level shifts in previous results including two-photon driving [15]. Simulation 1 was conducted using the same parameters as the experiment without modeling decoherence. Figure 2 (a) compares Simulation 1 and experimental results, with Simulation 1 giving  $\bar{\mathcal{F}} = 98.3 \pm 0.4\%$ . Simulations also show a drop in fidelity when increasing  $\Omega_{01}$  and  $\Omega_{12}$ , as well as a weak variation when scaling the drive voltage, as observed in the experiment. Numerical simulation of each gate in  $\mathcal{C}_3$  individually, and then averaging their respective fidelities, gave  $\bar{\mathcal{F}} = 98.4 \pm 1.08\%$ , with individual gate fidelities ranging from 95.8% to 99.9%. This shows that in addition to the average fidelity being high, each gate in  $\mathcal{C}_3$  is synthesized to high fidelity as well. The range in fidelity is also comparable to the range of fidelities from QPT.

Comparing the experiment against Simulation 1, we note that  $V_f$  from the simulation of  $4.00 \pm 0.09$  is significantly lower than both the experiment result and  $\text{Tr}(V\rho_{\text{dep}})$ . A likely cause for this is leakage out of the qutrit space  $\text{span}(\{|0\rangle, |1\rangle, |2\rangle\})$ . Figure 2 (b) shows the populations found in Simulation 1. These populations are used to determine the average leakage (seepage) per Clifford  $L_1$  ( $L_2$ ), and the adjusted average fidelity  $\bar{\mathcal{F}}_L$  following [23]. Simulation 1 gives  $L_1 = (1.36 \pm 0.82) \times 10^{-3}$ ,  $L_2 = (6.50 \pm 2.83) \times 10^{-3}$ , and  $\bar{\mathcal{F}}_L = 96.9 \pm 1.4\%$ . Since  $\bar{\mathcal{F}}_L$  is not significantly smaller than the simulated  $\bar{\mathcal{F}}$ , and

the small leakage approximation from [23] matches the simulated populations, leakage does not contribute significantly to the error in simulation.

To gain further insight into the role of leakage in the experiment, we modeled the measured homodyne voltage with additional components arising from higher states in Simulation 2. Simulation 2 indicates that the only significant populations of higher states are those for states 3 and 6, which arises due to the strength of matrix elements in the driving Hamiltonian. We take  $V_3$  and  $V_6$  as free parameters in the fit. The resulting  $V_3 = 4.69 \pm 1.15$  mV and  $V_6 = 6.89 \pm 1.83$  mV gave  $V_i = 5.37 \pm 0.03$  mV and  $V_f = 4.51 \pm 0.12$  mV, in line with experimental values. However, the optimization caused simulated  $\bar{\mathcal{F}}$  to drop from  $98.3 \pm 0.4\%$  to  $95.4 \pm 1.8\%$ , which does not match the experimental result. The uncertainty in the estimated  $V_3$  and  $V_6$  is also much larger than the experimentally-measured uncertainty of the homodyne voltages for the states in the qutrit space, suggesting that  $\bar{\mathcal{F}}$  depends weakly on these values.

The role of decoherence was analyzed based on a model that includes measured relaxation and excitation rates and dephasing in the qutrit space (see Supplemental Material). Adding decoherence to the simulations in Simulation 3 brought the spread of  $\langle V \rangle$  for  $l$  in line with experiment values, and it gave a  $V_f$  of  $4.17 \pm 0.04$  mV, with  $V_3$  and  $V_6$  set to 0. This indicates that decoherence further reduces the dependence of  $\bar{\mathcal{F}}$  on a non-zero  $V_3$  and  $V_6$ . This shows that contributions to the error from leakage and decoherence are small compared to coherent control errors.

To analyze coherent control error in the qutrit RB experiment, we investigate the connection between the error of Clifford group unitaries and the errors in the components  $R(\theta)_\phi^{mn}$ . For a noisy implementation  $\tilde{C} = \prod_n \tilde{R}_n$  of a qutrit gate  $C = \prod_n R_n$ , with  $\tilde{R}_n$  of noisy versions of ideal Givens rotations  $R_n$ , the gate error  $r(\tilde{C}, C) = 1 - \mathcal{F}(\tilde{C}, C)$  is approximately

$$r(\tilde{C}, C) \approx \sum_n r(\tilde{R}_n, R_n), \quad (2)$$

with  $r(\tilde{R}_n, R_n) = 1 - \mathcal{F}(\tilde{R}_n, R_n)$ . The approximation follows from modeling the error for a Givens rotation as an operator  $K_n = \tilde{R}_n R_n^\dagger$ , assuming  $K_n = \alpha_n I + \beta_n M_n$ , where  $\alpha_n$  is given by  $\arg \min_{x \in \mathbb{C}, |x| \leq 1} \|K_n - xI\|_\infty$ ,  $\beta_n = \|K_n - \alpha_n I\|_\infty$ , and  $M_n = \frac{1}{\beta_n} (K_n - \alpha_n I)$ . Relating  $\alpha_n$  and  $\beta_n$  to  $\mathcal{F}(\tilde{R}_n, R_n)$  and  $\mathcal{F}(\tilde{C}, C)$  using

$$\mathcal{F}(\tilde{V}, V) = \frac{\sum_{U_j \in \mathcal{P}_d} \text{Tr} \left( V^\dagger U_j V \tilde{V} U_j \tilde{V}^\dagger \right) + d^2}{d^2(d+1)} \quad (3)$$

for two unitaries  $V$  and  $\tilde{V}$  yields the approximation, assuming products of  $\beta_n$  are small. (See Supplemental Ma-

terial) Figure 4 (a) shows that Equation 2 holds numerically, and gets better as  $r(\tilde{C}, C)$  drops.

To understand the errors in individual Givens rotations, we numerically calculate the effective Hamiltonian  $H_{\text{eff}} = -\frac{i}{\tau} \ln \tilde{R}_n$ , where  $\tau$  is the effective time to implement  $R_n$  and  $\ln \tilde{R}_n$  is the matrix logarithm. The difference between  $H_{\text{eff}}$  and the ideal control Hamiltonian  $H_{\text{drive}}$  can be connected to errors introduced by the failure of the rotating wave approximation. Figure 4 (b) shows the error of the Givens rotations versus drive strength, showing that the error scales quadratically with the drive strength. The scaling of the error is consistent with additional terms in the effective Hamiltonian of the type

$$H_{\text{eff}} = H_{\text{drive}} + s_{mn} \sigma_z^{mn} \quad (4)$$

where  $s_{mn} \propto \Omega_{mn}^2$  characterizes the level shift due to ac-Stark and Bloch-Siegert shifts, and  $\sigma_z^{mn} = |m\rangle\langle m| - |n\rangle\langle n|$ . These terms are signatures of an ac-Stark shift on the transition not being driven, and a Bloch-Siegert shift on the level being driven [15]. Figure 4 (c) shows  $\text{Tr}(H_{\text{eff}} \sigma_z^{mn})$  for  $mn = 01$  and  $mn = 12$  for  $R(\pi)_0^{01}$  and Figure 4 (d) shows the results for  $R(\pi)_0^{12}$ . These show that  $\text{Tr}(H_{\text{eff}} \sigma_z^{mn})$  is proportional to  $\Omega^2$  as expected for a Stark shift. The leakage error identified in the RB analysis is also visible in simulation of the Givens rotations as non-negligible values of  $\langle 2|H_{\text{eff}}|3 \rangle$ ,  $\langle 1|H_{\text{eff}}|6 \rangle$ , and  $\langle 2|H_{\text{eff}}|6 \rangle$ . However, these terms are small compared to  $\text{Tr}(H_{\text{eff}} \sigma_z^{mn})$ , confirming that contribution of leakage to the control error is small compared to level shifts. Note that level shift error is much more significant for qutrit RB than qubit RB, since the level shift is a coherent error on levels used to store information, compared to an incoherent error on levels not used to store information in qubit RB [24].

In conclusion, we have demonstrated control sufficient to synthesize the qutrit Clifford group  $\mathcal{C}_3$  to 99% fidelity, using a universal method for gate decomposition into Givens rotations. While leakage out of the qutrit space and decoherence contribute to the measured gate errors, level shifts due to off resonant coupling to states outside the driven two-dimensional subspace corresponding to each Givens rotation are the dominant source of error. In future work it will be important to explore application of level shift corrections, as done in Ref. [15], and more generally design optimal control pulses that mitigate both level shifts and leakage. These results establish randomized benchmarking as a tool to understand superconducting qutrit control and pave the way towards using superconducting qudits in quantum information tasks.

We thank the University of Waterloo Quantum Nanofab team members for their help during device fabrication. We thank Sahel Ashhab for general discussions on level shifts. We acknowledge support from NSERC, the Canada Foundation for Innovation (CFI), the Ontario

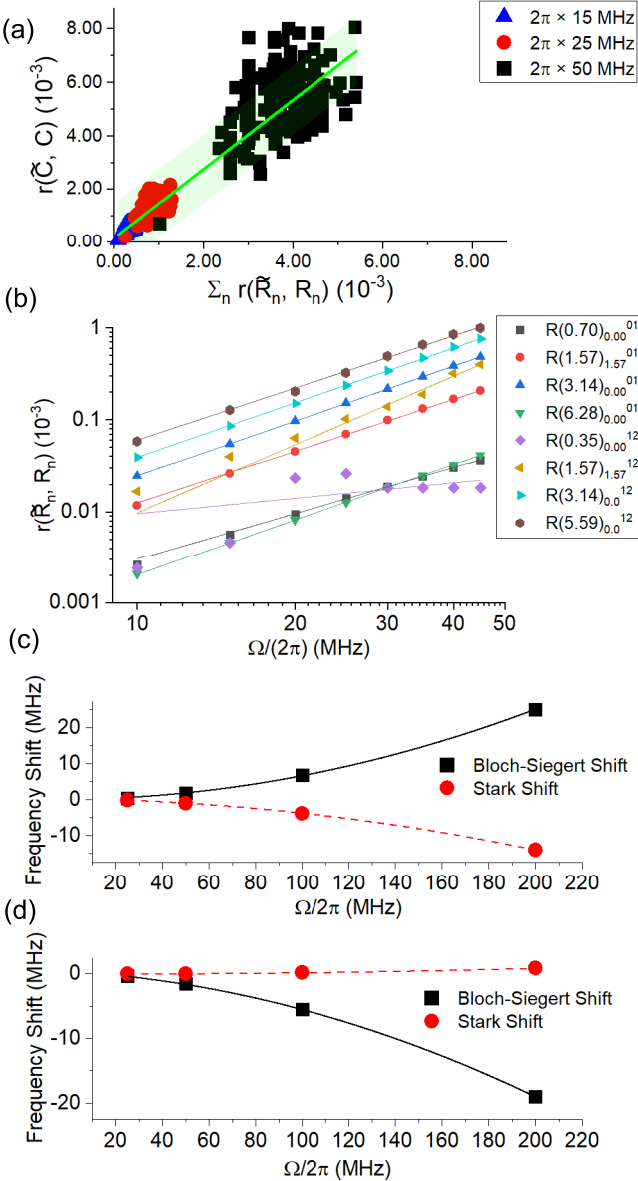


FIG. 4. (a) The error of the Clifford gate versus the sum of the errors of the component Givens rotations for  $C_3$  at various drive frequencies. The line of best fit and 95% prediction bands are also shown. (b) The error versus the drive frequency for a set of Givens rotations, at  $\Omega = 2\pi \times 50$  MHz. The Stark shift and Bloch-Siegert Shift shown for (c)  $R(\pi)^{01}$  and for (d)  $R(\pi)^{12}$ . The lines in (c) and (d) show quadratic fits.

Ministry of Research and Innovation, Industry Canada, and the Canadian Microelectronics Corporation (CMC).

*Note added:* During the completion of our manuscript, we became aware of a recent related manuscript in qutrit randomized benchmarking [25].

<sup>†</sup> mayurtalan@uwaterloo.ca

<sup>‡</sup> alupascu@uwaterloo.ca

- [1] F. Arute, K. Arya, R. Babbush, D. Bacon, *et al.*, *Nature* **574**, 505 (2019).
- [2] J. S. Otterbach, R. Manenti, N. Alidoust, A. Bestwick, *et al.*, (2017), arXiv:1712.05771 [quant-ph].
- [3] A. D. Corcoles, A. Kandala, A. Javadi-Abhari, D. T. McClure, *et al.*, (2019), arXiv:1910.02894 [quant-ph].
- [4] K. Wright, K. M. Beck, S. Debnath, J. M. Amini, *et al.*, *Nature Communications* **10**, 5464 (2019).
- [5] E. T. Campbell, *Physical Review Letters* **113**, 230501 (2014).
- [6] E. T. Campbell, H. Anwar, and D. E. Browne, *Physical Review X* **2**, 041021 (2012).
- [7] H. Anwar, B. J. Brown, E. T. Campbell, and D. E. Browne, *New Journal of Physics* **16**, 063038 (2014).
- [8] A. Krishna and J.-P. Tillich, *Physical Review Letters* **123**, 070507 (2019).
- [9] A. R. Shlyakhov, V. V. Zemlyanov, M. V. Suslov, A. V. Lebedev, *et al.*, *Physical Review A* **97**, 022115 (2018).
- [10] M. V. Suslov, G. B. Lesovik, and G. Blatter, *Physical Review A* **83**, 052317 (2011).
- [11] F. Bouchard, R. Fickler, R. W. Boyd, and E. Karimi, *Science Advances* **3**, e1601915 (2017).
- [12] C. M. Dawson and M. A. Nielsen, *Quantum Information & Computation* **6**, 81 (2006).
- [13] M. A. Yurtalan, J. Shi, G. J. K. Flatt, and A. Lupascu, arXiv:2008.00593 [quant-ph] (2020), arXiv:2008.00593 [quant-ph].
- [14] S. G. Schirmer, A. D. Greentree, V. Ramakrishna, and H. Rabitz, *J. Phys. A: Mathematical and General* **35**, 8315 (2002).
- [15] M. A. Yurtalan, J. Shi, M. Kononenko, A. Lupascu, and S. Ashhab, arXiv:2003.04879 [quant-ph] (2020), arXiv:2003.04879 [quant-ph].
- [16] I. L. Chuang and M. A. Nielsen, *Journal of Modern Optics* **44**, 2455 (1997).
- [17] M. A. Nielsen, *Physics Letters A* **303**, 249 (2002).
- [18] A. N. Glaudell, N. J. Ross, and J. M. Taylor, *Annals of Physics* **406**, 54 (2019).
- [19] J. Emerson, R. Alicki, and K. Zyczkowski, *J. Opt. B: Quantum Semiclass. Opt.* **7**, S347 (2005).
- [20] E. Magesan, J. M. Gambetta, and J. Emerson, *Physical Review Letters* **106**, 180504 (2011).
- [21] M. Jafarzadeh, Y.-D. Wu, Y. R. Sanders, and B. C. Sanders, *New Journal of Physics* **22**, 063014 (2020).
- [22] D. Gottesman, in *Quantum Computing and Quantum Communications*, Lecture Notes in Computer Science, edited by C. P. Williams (Springer, Berlin, Heidelberg, 1999) pp. 302–313.
- [23] C. J. Wood and J. M. Gambetta, *Physical Review A* **97**, 032306 (2018), arXiv:1704.03081.
- [24] Z. Chen, J. Kelly, C. Quintana, R. Barends, *et al.*, *Physical Review Letters* **116**, 020501 (2016).
- [25] A. Morvan, V. V. Ramasesh, M. S. Blok, J. M. Kreikebaum, K. O’Brien, *et al.*, (2020), arXiv:2008.09134 [quant-ph].

\* mkononen@uwaterloo.ca

# Supplemental Material for “Characterization of Control in a Superconducting Qutrit Using Randomized Benchmarking”

## EXPERIMENT DETAILS

The device is manufactured using a planar process described in Ref. [S1] (Supplemental Material). The device is capacitively coupled to a coplanar waveguide resonator for dispersive readout, and to a transmission line terminated by a capacitor for control. The device is placed in a microwave package and mounted in a dilution cryostat. Experiments are done with the device operated at its flux symmetry point, with the required flux provided by an external coil. The measured transition frequencies are  $\omega_{01} = 2\pi \times 1.15$  GHz,  $\omega_{12} = 2\pi \times 5.69$  GHz, and  $\omega_{23} = 2\pi \times 5.12$  GHz, where  $\omega_{mn}$  is the frequency of the transition between states  $m$  and  $n$ . The Rabi frequency was measured versus the amplitude of the applied ac voltage for each transition, and had the expected linear dependence with a slope  $K_{mn}$  for transition  $m - n$ . For the 01 (12) transition, the coefficient is  $1021 \pm 4$  MHz V $^{-1}$  ( $411 \pm 4$  MHz V $^{-1}$ ). Readout is done with a resonator with a resonance frequency  $2\pi \times 6.71955$  GHz and full-width at half-maximum (FWHM) of  $2\pi \times 784$  kHz, coupling to the lowest two levels of the device with a Jaynes-Cummings interaction strength of  $g_{01} = 2\pi \times 11.6$  MHz. We use the methods in Ref. [S2] to measure the thermal state  $\rho_{\text{th}} = (0.703 \pm 0.007) |0\rangle\langle 0| + (0.297 \pm 0.007) |1\rangle\langle 1|$  and the voltage levels  $V_0 = 6.57 \pm 0.06$  mV,  $V_1 = 2.47 \pm 0.03$  mV, and  $V_2 = 4.73 \pm 0.05$  mV. The ground state population of the thermal state  $\langle 0|\rho_{\text{th}}|0\rangle$  is consistent with an effective temperature of  $64 \pm 2$  mK.

We extract the coherence times of the device used as a qutrit following Ref. [S2]. Table S1 shows the relaxation ( $m > n$ ) and excitation ( $m < n$ ) rates  $\Gamma_1^{mn}$  and the Ramsey dephasing rates  $\Gamma_2^{mn}$  for all pairs of the qutrit energy levels [S3].

TABLE S1. The decoherence rates measured in the qutrit space.

Rate	Value (Hz)
$\Gamma_1^{10}$	$1.62 \times 10^4$
$\Gamma_1^{01}$	$5.40 \times 10^3$
$\Gamma_1^{21}$	$3.15 \times 10^5$
$\Gamma_1^{12}$	$1.50 \times 10^4$
$\Gamma_1^{20}$	$2.16 \times 10^4$
$\Gamma_1^{02}$	$1.50 \times 10^3$
$\Gamma_2^{01}$	$2.04 \times 10^5$
$\Gamma_2^{12}$	$2.38 \times 10^5$
$\Gamma_2^{02}$	$1.82 \times 10^5$

## THE GATE DECOMPOSITION

Our gate decomposition, based on Ref. [S4], decomposes a general  $d$ -dimensional qudit gate  $U$  into a product of rotations  $R(\theta)_{\phi}^{mn}$ , where  $\theta$  is the rotation angle,  $\phi$  is the rotation phase, and  $mn$  is the two dimensional subspace where this rotation acts. In the first step, a set of Given rotations is chosen such that their application leads to transforming  $U$  to a diagonal form. Each Givens rotations is tailored to cancel  $\langle m|R(\theta)_{\phi}^{mn}U'|k\rangle$ , with  $U'$  the unitary obtained by applying the previous rotations to  $U$ , by choosing

$$\sin \theta = \frac{|\langle m|U'|k\rangle|}{\sqrt{|\langle m|U'|k\rangle|^2 + |\langle n|U'|k\rangle|^2}}, \quad (\text{S1})$$

and

$$e^{i\phi} = i \frac{(\langle m|U'|k\rangle)^{\dagger} \langle n|U'|k\rangle}{|\langle m|U'|k\rangle| |\langle n|U'|k\rangle|}. \quad (\text{S2})$$

A total of  $\frac{1}{2}d(d-1)$  rotations are needed, equal to the number of elements of  $U$  in the upper triangular region.

TABLE S2. The Givens Rotation Decomposition for  $H_3$ ,  $S_3$ ,  $X_3$ , and  $Z_3$ . Solid red areas represent 12 rotations and black areas represent 01 rotations

Pulse Number	$H_3$	$S_3$	$X_3$	$Z_3$
0	$R(1.5708)_{2.61799}^{01}$	$R(1.5708)_{1.5708}^{01}$	$R(3.14159)_{0.0}^{12}$	$R(1.5708)_{1.5708}^{12}$
1	$R(1.91063)_{-3.66519}^{12}$	$R(1.39626)_{3.14159}^{01}$	$R(3.14159)_{0.0}^{01}$	$R(4.18879)_{0.0}^{12}$
2	$R(1.5708)_{1.0472}^{01}$	$R(1.5708)_{-1.5708}^{01}$	$R(1.5708)_{1.5708}^{01}$	$R(1.5708)_{-1.5708}^{12}$
3	$R(1.5708)_{1.5708}^{01}$	$R(1.5708)_{1.5708}^{12}$	$R(6.28319)_{-3.14159}^{01}$	
4	$R(4.18879)_{-3.14159}^{01}$	$R(2.79253)_{-3.14159}^{12}$	$R(1.5708)_{-1.5708}^{01}$	
5	$R(1.5708)_{-1.5708}^{01}$	$R(1.5708)_{-1.5708}^{12}$	$R(1.5708)_{1.5708}^{12}$	
6	$R(1.5708)_{1.5708}^{12}$		$R(3.14159)_{-3.14159}^{12}$	
7	$R(1.0472)_{-3.14159}^{12}$		$R(1.5708)_{-1.5708}^{12}$	
8	$R(1.5708)_{-1.5708}^{12}$			

In the second step, phase gates in  $d - 1$  subspaces are needed to reduced the diagonal unitary to identity. Each of these phase gates is of the form

$$\exp(i\beta\sigma_z^{mn}) = R\left(-\frac{\pi}{2}\right)^{mn} R(2\beta)_0^{mn} R\left(\frac{\pi}{2}\right)^{mn}, \quad (\text{S3})$$

where  $\sigma_z^{mn} = |m\rangle\langle m| - |n\rangle\langle n|$ . A total of  $3(d - 1)$  Givens rotations is needed in this step.

In the case of a qutrit gate  $U \in \text{SU}(3)$ , the off-diagonal components are cancelled out by three rotations  $R(\theta_1)_{\phi_1}^{01}$ ,  $R(\theta_2)_{\phi_2}^{12}$ , and  $R(\theta_3)_{\phi_3}^{01}$ .  $R(\theta_1)_{\phi_1}^{01}$  implements  $\langle 0|U|2\rangle$ ,  $R(\theta_2)_{\phi_2}^{12}$  implements  $\langle 1|U|2\rangle$ , and  $R(\theta_3)_{\phi_3}^{01}$  implements  $\langle 0|U|1\rangle$ . Next, two phase gates for subspaces 01 and 12 are needed to transform the remaining diagonal unitary into the identity.

Each  $R(\theta)_{\phi}^{mn}$  is mapped to a single pulse with a cosine rise and fall envelope. The maximum amplitude of the pulse is set by the drive strength  $\Omega_{mn}$ . If  $\theta$  is too small to be implemented by a pulse of length  $t_{\text{rise}} + t_{\text{fall}}$  at a drive strength  $\Omega_{mn}$ , then the drive strength is reduced so that the pulse length is at least  $t_{\text{rise}} + t_{\text{fall}}$ . Table S2 gives the Givens rotation decomposition for  $H_3$ ,  $S_3$ ,  $X_3$ , and  $Z_3$ . Figure S1 gives the AWG waveforms implementing these gates at a drive strength  $\Omega = \Omega_{01} = \Omega_{12} = 50$  MHz.

## NUMERICAL SIMULATION OF DEVICE DYNAMICS

The circuit Hamiltonian, derived by the model presented in earlier work [S2], together with the drive has the form  $H(V(t)) = H_{\text{static}} + H_{\text{drive}}(V(t))$ , where  $H_{\text{static}} = \sum_{j=1}^{d-1} \omega_{0j} |j\rangle\langle j|$  has the diagonal terms and  $H_{\text{drive}}(V(t)) = \sum_{\substack{i,j=0 \\ i \neq j}}^{d-1} V(t) (g_{ij} |i\rangle\langle j| + \text{h.c.})$  describes time-dependent control with the voltage  $V(t)$  at control pad of the device. The transition frequencies  $\omega_{0j}$  and the transition matrix elements  $g_{ij}$  of the voltage operator are calculated from the circuit model fitted to the experimental data. The Hilbert space is truncated to the lowest 7 levels, owing to the agreement between the simulation and previous multi-level control experiments including two-photon Rabi oscillations [S1]. The decoherence model consists of Lindblad operators of the form  $\sqrt{\Gamma_1^{mn}} |m\rangle\langle n|$  for relaxation/excitation, and  $\sqrt{\Gamma_2^{mn}/2} (|m\rangle\langle m| - |n\rangle\langle n|)$  for dephasing. To propagate  $\rho(t)$ , the Lindblad master equation [S5, Sec. 8.4.1] is solved numerically in qutip [S6]. To propagate uncertainties in  $P_{\text{th},0}$ , and  $V_n = \langle n|V|n\rangle$ , one simulation is done with  $|0\rangle\langle 0|$  as the initial state, another is done with  $|1\rangle\langle 1|$  as the initial state, and the results are then added together. For numerical simulations of Clifford gates and Givens rotations, we calculate the corresponding propagator at the end of the decomposition of the gate, and compare simulated propagators to ideal propagators. The AWG waveform voltage is related to the voltage at the device control pad by scaling the voltage of 01 and 12 pulses by their respective transfer coefficients  $c_{01} = 5.84 \times 10^{-3}$  and  $c_{12} = 7.02 \times 10^{-4}$ . These coefficients are determined by simulating a Rabi experiment, and matching the Rabi frequency with the experimentally-measured value.

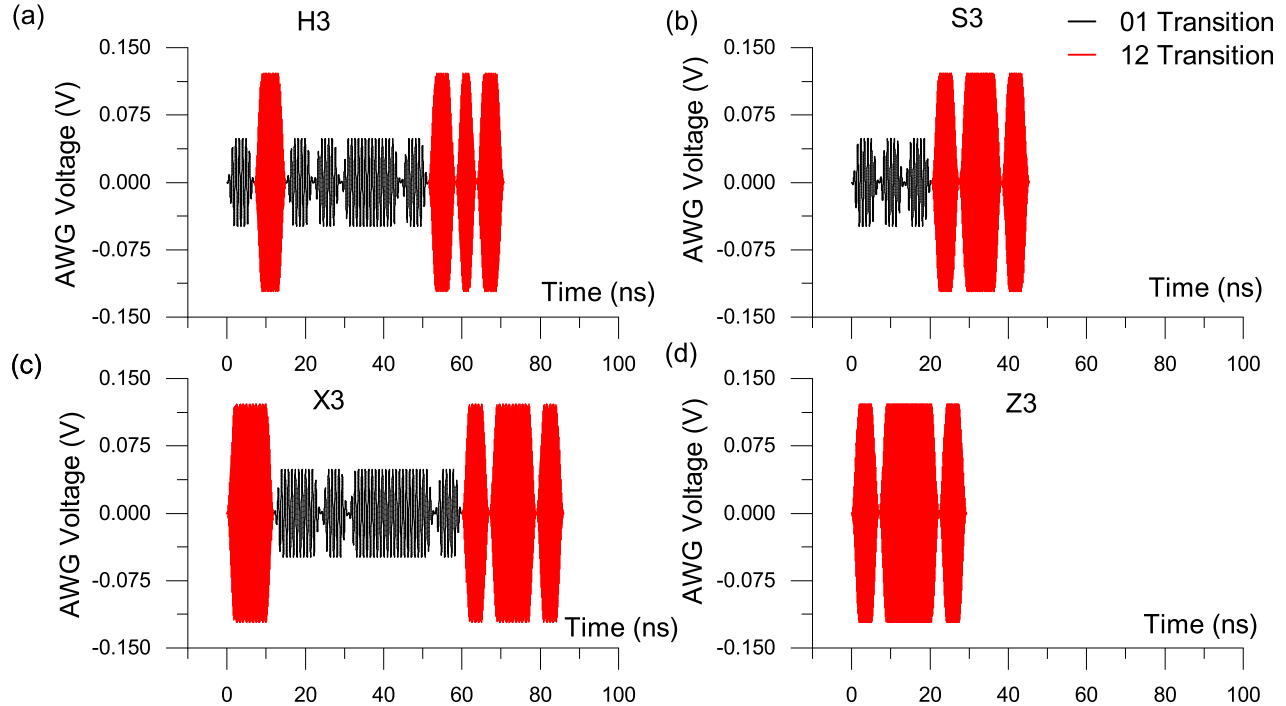


FIG. S1. The waveforms implementing the qutrit gates  $H_3$  (a),  $S_3$  (b),  $X_3$  (c), and  $Z_3$  (d). Black areas indicate 01 transitions and read areas indicated 12 transitions.

### CALCULATION OF GATE FIDELITY

Following [S7], the gate fidelity  $\mathcal{F}(\tilde{\mathcal{U}}, U)$ , where  $\tilde{\mathcal{U}}$  is a noisy implementation of  $U$ , is

$$\mathcal{F}(\tilde{\mathcal{U}}, U) = \frac{1}{d^2(d+1)} \sum_{P \in \mathcal{P}_d} \text{Tr} \left( P^\dagger U^\dagger \tilde{\mathcal{U}}(P) U \right) + \frac{1}{d+1}, \quad (\text{S4})$$

where  $\mathcal{P}_d$  is the Pauli group defined on a  $d$ -dimensional Hilbert space [S8]. To find the gate fidelity for the qutrit subspace in the simulated seven-dimensional Hilbert space, the elements of  $\mathcal{P}_3$  are expanded into 7-dimensional operators by padding the matrices with zeroes such that  $P \in \mathcal{P}_3$  occupied the top-left  $3 \times 3$  block.  $\mathcal{F}(\tilde{\mathcal{U}}, U)$  is then found using equation S4 with  $d = 3$ . This is done because  $\mathcal{P}_3$  is a basis for writing down the maximally-entangled qutrit state  $|\phi\rangle = \frac{1}{\sqrt{3}}(|0\rangle|0\rangle + |1\rangle|1\rangle + |2\rangle|2\rangle)$ , and equation S4 is derived via

$$\mathcal{F}(\tilde{\mathcal{U}}, U) = \frac{dF_e(U^\dagger \circ \tilde{\mathcal{U}}) + 1}{d+1}, \quad (\text{S5})$$

where the entanglement fidelity  $F_e = \langle \phi | I_3 \otimes (U^\dagger \circ \tilde{\mathcal{U}}) | \phi \rangle$  [S7], and  $I_3 = |0\rangle\langle 0| + |1\rangle\langle 1| + |2\rangle\langle 2|$ . Since the qutrit maximally entangled state has no components outside the lowest three levels, the elements of  $\mathcal{P}_3$  cannot have support outside the space spanned by the lowest three levels. This also means  $\mathcal{P}_3$  elements that are unitary in 3 dimensions are not unitary in 7 dimensions.

### APPROXIMATING THE FIDELITY OF CLIFFORD GATES FROM GIVENS ROTATIONS

Let  $C$  represent an ideal Clifford gate and  $\tilde{C}$  represent its error-prone implementation.  $\tilde{C}$  is  $\prod_n \tilde{R}_n$ , where  $\tilde{R}_n = K_n G_n$  is a noisy implementation of an ideal Givens rotation  $R_n$  with error  $K_n$ . Assume  $K_n = \alpha_n I + \beta_n M_n$ , where  $\alpha_n \in \mathbb{C}$ ,  $\beta \in \mathbb{R}$ , and  $M_n$  is an operator.  $I$  is the identity operator.  $\alpha_n$  is the complex number minimizing  $\|K_n - \alpha_n I\|_\infty$ , where

$\|A\|_\infty$  is the magnitude of the largest eigenvalue of an operator  $A$ .  $\beta_n = \|K_n - \alpha_n I\|_\infty$  and  $M_n = \frac{1}{\beta_n}(K_n - \alpha_n I)$ . The zeroth-order approximation to the fidelity  $\mathcal{F}_0(\tilde{C}, C)$  assumes  $\beta_n$  is small. The fidelity then simplifies as

$$\mathcal{F}_0(\tilde{C}, C) = \mathcal{F} \left( \prod_n K_n R_n, \prod_n R_n \right) \Big|_{\beta_n=0} \quad (\text{S6})$$

$$= \mathcal{F}_0 \left( \prod_n \alpha_n \prod_n R_n, \prod_n R_n \right) \quad (\text{S7})$$

$$= \mathcal{F}_0 \left( \prod_n \alpha_n I, I \right) \quad (\text{S8})$$

$$= \frac{1}{d^2(d+1)} \sum_j \text{Tr} \left( \left( \prod_n \alpha_n U_j \prod_n \alpha_n^* U_j^\dagger \right) \right) + \frac{1}{d+1} \quad (\text{S9})$$

$$= \frac{1}{d^2(d+1)} \prod_n |\alpha_n|^2 \sum_{j=1}^{d^2} \text{Tr} \left( U_j U_j^\dagger \right) + \frac{1}{d+1} \quad (\text{S10})$$

$$= \frac{1}{d^2(d+1)} \prod_n |\alpha_n|^2 \sum_{j=1}^{d^2} \text{Tr} \left( I_3 \right) + \frac{1}{d+1} \quad (\text{S11})$$

$$= \frac{d \prod_n |\alpha_n|^2 + 1}{d+1}. \quad (\text{S12})$$

Let  $r_0(\tilde{C}, C) = 1 - \mathcal{F}_0(\tilde{C}, C)$  represent the zeroth-order approximation to the error. For a single Givens rotation  $\tilde{R}_n$ ,  $\alpha_n$  is related to  $r_0(\tilde{R}_n, R_n)$  by

$$|\alpha_n|^2 = 1 - \frac{d+1}{d} r_0(\tilde{R}_n, R_n). \quad (\text{S13})$$

The zeroth-order error for a Clifford gate is then

$$r_0(\tilde{C}, C) = \left( \frac{d}{d+1} \right) \left( 1 - \prod_n \left( 1 - \left( \frac{d+1}{d} \right) r_0(\tilde{R}_n, R_n) \right) \right). \quad (\text{S14})$$

Since  $r_0(\tilde{R}_n, R_n)$  is small, one can make the approximation

$$\prod_n \left( 1 - \left( \frac{d+1}{d} \right) r_0(\tilde{R}_n, R_n) \right) \approx 1 - \left( \frac{d+1}{d} \right) \sum_n r_0(\tilde{R}_n, R_n), \quad (\text{S15})$$

giving  $r_0(\tilde{C}, C) \approx \sum_n r_0(\tilde{R}_n, R_n)$ . If  $\beta$  is small, then  $r(\tilde{C}, C) \approx \sum_n r(\tilde{R}_n, R_n)$ .

Consider a  $\tilde{C}$  made of two Givens rotations, such that  $\tilde{C} = K_2 R_2 K_1 R_1$ . To get the first-order approximation to the fidelity  $\mathcal{F}_1(\tilde{C}, C)$ , assume any terms with more than one  $\beta$  are negligible when taking the product  $U_j^\dagger C^\dagger \tilde{C} U_j \tilde{C}^\dagger C$ . The approximation is

$$U_j^\dagger C^\dagger \tilde{C} U_j \tilde{C}^\dagger C \approx \alpha_2 \alpha_1 \alpha_1^* \alpha_2^* \left( I + U_j^\dagger R_1^\dagger R_2^\dagger \frac{\beta_2 M_2}{\alpha_2} R_2 R_1 U_j + U_j^\dagger R_1^\dagger \frac{\beta_1 M_1}{\alpha_1} R_1 U_j + I_3 \frac{\beta_1 M_1^\dagger}{\alpha_1^*} + I_3 R_1^\dagger \frac{\beta_2 M_2^\dagger}{\alpha_2^*} R_1 \right). \quad (\text{S16})$$

Substituting this into equation S4 gives

$$\mathcal{F}_1(\tilde{C}, C) = \frac{d \prod_n |\alpha_n|^2 + 1}{d+1} + \frac{\prod_n |\alpha_n|^2}{d+1} \left( \text{Tr} \left( \beta_1 \left( \frac{M_1}{\alpha_1} + \frac{M_1^\dagger}{\alpha_1^*} \right) I_3 \right) + \text{Tr} \left( \beta_2 \left( \frac{M_2}{\alpha_2} + \frac{M_2^\dagger}{\alpha_2^*} \right) I_3 \right) \right), \quad (\text{S17})$$

which generalizes to

$$\mathcal{F}_1(\tilde{C}, C) = \mathcal{F}_0(\tilde{C}, C) + \frac{\prod_n |\alpha_n|^2}{d+1} \sum_n \text{Tr} \left( \beta_n \left( \frac{M_n}{\alpha_n} + \frac{M_n^\dagger}{\alpha_n^*} \right) I_3 \right) \quad (\text{S18})$$

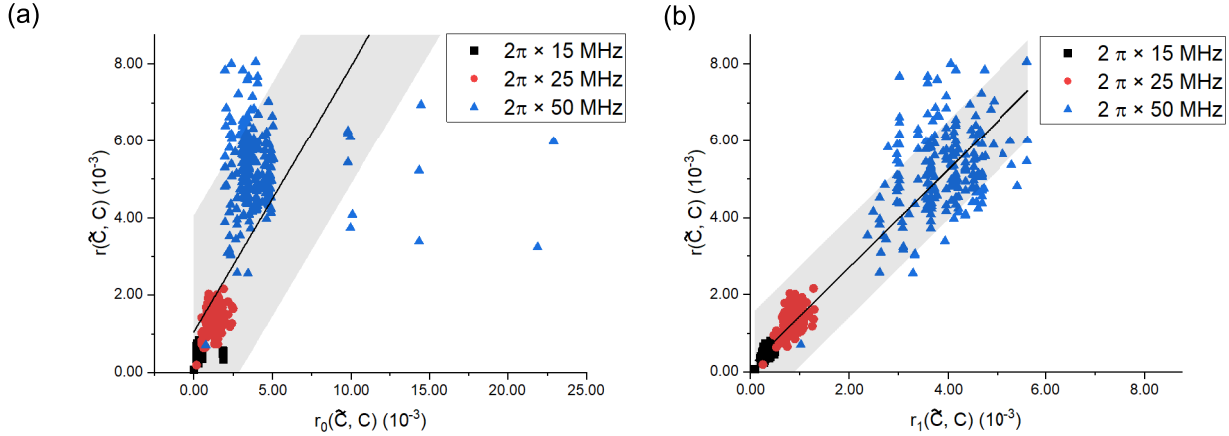


FIG. S2. The simulated error for each Clifford gate versus its (a) zeroth-order estimate and (b) first-order estimate. The line of best fit and 95% prediction bands are shown as well.

Figure S2 shows  $r(\tilde{C}, C)$  versus  $r_0(\tilde{C}, C)$  and  $r_1(\tilde{C}, C)$ , for the same Clifford gates as in Figure 4 (a) in the main text. The first-order approximation improves the estimate of  $\mathcal{F}(\tilde{C}, C)$ , as can be seen by the 95% prediction band narrowing.

#### EFFECTIVE HAMILTONIAN CALCULATION

To find the Hamiltonian  $H_{\text{eff}}$  such that  $U = \exp(-iH_{\text{eff}}\tau)$ , the objective function  $1 - \mathcal{F}(\tilde{U}, \exp(-iH_{\text{eff}}\tau))$  is minimized over the space of possible Hamiltonians. In the minimization, the gate fidelity  $\mathcal{F}$  is taken over seven dimensions, not three, so that the effective Hamiltonian replicates the dynamics outside the qutrit space as well as inside. The initial condition for this minimization is an ideal Hamiltonian  $\tilde{H}$ . The Hilbert space of Hamiltonians is parameterized by the Generalized Gell-Mann matrices  $G_k$ , giving  $\tilde{H} = \sum_k \alpha_k G_k$  and  $H_{\text{eff}} = \sum_k \beta_k G_k$  [S9].  $\beta_k$  is constrained to prevent spurious  $2\pi$  rotations from being introduced.

\* mkononen@uwaterloo.ca

† mayurtalan@uwaterloo.ca

‡ alupascu@uwaterloo.ca

[S1] M. A. Yurtalan, J. Shi, M. Kononenko, A. Lupascu, and S. Ashhab, arXiv:2003.04879 [quant-ph] (2020), arXiv:2003.04879 [quant-ph].

[S2] M. A. Yurtalan, J. Shi, G. J. K. Flatt, and A. Lupascu, arXiv:2008.00593 [quant-ph] (2020), arXiv:2008.00593 [quant-ph].

[S3] M. H. Levitt, *Spin Dynamics: Basics of Nuclear Magnetic Resonance*, 2nd ed. (Wiley, Chichester, England ; Hoboken, NJ, 2008).

[S4] S. G. Schirmer, A. D. Greentree, V. Ramakrishna, and H. Rabitz, J. Phys. A: Mathematical and General **35**, 8315 (2002).

[S5] M. A. Nielsen and I. L. Chuang, *Quantum Computation and Quantum Information*, first south asia edition ed. (Cambridge University Press, Cambridge, 2013).

[S6] J. R. Johansson, P. D. Nation, and F. Nori, Computer Physics Communications **184**, 1234 (2013).

[S7] M. A. Nielsen, Physics Letters A **303**, 249 (2002).

[S8] D. Gottesman, in *Quantum Computing and Quantum Communications*, Lecture Notes in Computer Science, edited by C. P. Williams (Springer, Berlin, Heidelberg, 1999) pp. 302–313.

[S9] R. A. Bertlmann and P. Krammer, Journal of Physics A: Mathematical and Theoretical **41**, 235303 (2008).